# Using Gaussian process regression and stable isotopologues of water vapor to estimate shallow convective moistening in the southeastern Pacific marine stratocumulus region

Joseph Galewsky[1], Camille Risi[2], and Hélène Brogniez[3]

[1]University of New Mexico
[2]Laboratoire de Météorologie Dynamique, France
[3]Laboratoire atmosphères, observations spatiales

November 26, 2022

**Abstract**

Convective mixing in the lower free troposphere (LFT) and its response to climate change are at the heart of low-cloud feedbacks in projections of future warming, but are challenging to diagnose from observations. The stable isotopic composition of water vapor in the LFT is a sensitive recorder of shallow convective moistening, and can potentially provide independent constraints on shallow convective processes. In-situ and remote sensing measurements from the southeast Pacific marine stratocumulus region and an isotope-enabled general circulation model (GCM) are used along with Gaussian process regression (GPR) to explore the utility of stable isotope measurements and simulations for improved estimates of shallow convective moistening tendencies in marine stratocumulus settings. We train the GPR algorithm on conventional and isotopic fields from a GCM (LMDZ5B) from the SE Pacific marine stratocumulus region and assess the algorithm on out-of-sample GCM output. The GPR trained on isotopic fields yields better estimates of shallow convective moistening tendencies than GPR trained only on conventional meteorological fields. Climate change is not well-captured if the GPR is trained only on the control climate, but performs much better if the training data include samples from both cool and warm climates, and is also reasonably well-captured if the GPR is only trained on the warm climate. The GPR algorithm is applied to isotopic and conventional measurements from the SE Pacific and yields realistic estimates of shallow convective moistening tendencies. Linking machine learning with isotopic simulations and measurements provides a unique and potentially useful framework for bridging GCMs and observations.

# Using Gaussian process regression and stable isotopologues of water vapor to estimate shallow convective moistening in the southeastern Pacific marine stratocumulus region

**Joseph Galewsky[1], Camille Risi[2], Hélène Brogniez[3]**

[1]Department of Earth and Planetary Sciences, University of New Mexico
[2]Le Laboratoire de Météorologie Dynamique, Paris, France
[3]LATMOS/IPSL, UVSQ Université Paris-Saclay, Sorbonne Université, CNRS, Guyancourt, France

**Key Points:**

- Gaussian process regression (GPR) trained with water vapor isotopic fields gives accurate and parsimonious estimates of shallow convective moistening tendencies.
- GPR trained on climate model output and applied to observations yields physically realistic estimates of moistening tendencies.
- The inclusion of stable isotope fields in training datasets yields measurable improvements over purely conventional training datasets.

Corresponding author: Joseph Galewsky, galewsky@unm.edu

## Abstract

Convective mixing in the lower free troposphere (LFT) and its response to climate change are at the heart of low-cloud feedbacks and associated uncertainties in projections of future warming, but are challenging to diagnose from observations. The stable isotopic composition of water vapor in the LFT is a sensitive recorder of shallow convective moistening, and can potentially provide independent constraints on shallow convective processes. Here, in-situ and remote sensing measurements from the southeast Pacific marine stratocumulus region and an isotope-enabled general circulation model (GCM) are used along with Gaussian process regression (GPR) to explore the utility of using stable isotope measurements and simulations for improved estimates of shallow convective moistening tendencies in marine stratocumulus settings. We train the GPR algorithm on both conventional and isotopic fields from a GCM (LMDZ5B) from the SE Pacific marine stratocumulus region and assess the algorithm on out-of-sample GCM output. The GPR trained on isotopic fields yields better estimates of shallow convective moistening tendencies than GPR trained only on conventional meteorological fields. As in other studies, climate change is not well-captured if the GPR is trained only on the control climate, but performs much better if the training data include samples from both cool and warm climates, and is also reasonably well-captured if the GPR is only trained on the warm climate. The GPR algorithm is applied to isotopic and conventional measurements from the SE Pacific and yields realistic estimates of shallow convective moistening tendencies. Linking machine learning with isotopic simulations and measurements provides a unique and potentially useful framework for bridging GCMs and observations.


## 1 Plain Language Summary

Understanding the response of low clouds to climate change is at the heart of improved constraints on future warming. Climate models show a wide range of responses, but generally show that a reduction in low-cloud cover can exacerbate greenhouse warming. Understanding the processes that impact these low-cloud feedbacks in climate models is important, but linking the insights from modeling studies to observations is problematic because the governing processes are very difficult to measure in the atmosphere. Here we show how a new technique for modeling the stable isotopic composition of water vapor, which can be readily measured in the atmosphere, may yield a reliable proxy for the convective processes that are thought to govern low-cloud feedbacks.

## 2 Introduction

The potential for large changes in low-cloud fractions (LCF) in marine low-cloud regions as the climate warms has been identified as one of the leading uncertainties in climate change projections (Sherwood et al., 2014; Bony & Dufresne, 2005; Bony et al., 2004). The strong inversion at the top of the MBL in these regions limits mixing between the MBL and the lower free troposphere (LFT), leading to a more humid and a cloudier MBL. A reduction in the strength of the inversion is associated with enhanced export of water vapor from the MBL, a drier MBL, a more humid LFT, and reduced cloud cover (Brient et al., 2016; Zhang et al., 2013). These effects are modulated by variations in SST. In the absence of a change in inversion strength, an increase in SST may lead to a drier and less cloudy MBL through increased latent heat fluxes and enhanced buoyancy-driven mixing with the free troposphere (Rieck et al., 2012; Chung & Teixeira, 2012). An increase in SST may lead to a larger humidity contrast between the MBL and the LFT as the MBL moistens at a higher rate than the LFT, leading to reduced LCF as the relatively drier air is entrained into the MBL (Dussen et al., 2015). The mixing processes that govern much of the variability of LCF in marine low-cloud regions can be diagnosed from climate model output and can be inferred from observations, but such inferences remain challenging with conventional meteorological datasets (Lamer et al., 2015; Vogel et al., 2020). Thus, there is an ongoing need for innovative and complementary techniques for estimating mixing processes within the LFT.

Stable isotopes in atmospheric water vapor carry a fingerprint of the history of phase changes and mixing between airmasses (Galewsky et al., 2016) and in principle could be useful for improved inference of convective mixing. Recent studies (Galewsky, 2018b, 2018a) have taken advantage of in situ measurements of water vapor mixing ratio and isotopic composition from the lower and middle free troposphere to develop new methods for diagnosing mixing between the MBL and the LFT. The studies of Galewsky (2018b, 2018a) used an inverse modeling approach based on genetic algorithms (Galewsky & Rabanus, 2016) to partition the joint distribution of total mixing ratio ($q$) and $\delta$D into a dry, isotopically-depleted airmass associated with a last-saturation temperature in the upper troposphere that is mixed with a moist, isotopically-enriched airmass, interpreted to represent water vapor transported from the MBL into the LFT. While those studies yielded results that are internally consistent, they relied on nonunique interpretations of isotopic data and did not leverage additional observational datasets that may provide additional constraints on mixing estimates.

In recent years, there has been substantial interest in the use of machine learning (ML) algorithms in climate models, primarily within the context of improving physics parameterizations (O'Gorman & Dwyer, 2018; Gentine et al., 2018; Brenowitz & Bretherton, 2018), but ML approaches have also been used for building improved understanding of underlying physical processes in the climate system (Ukkonen & Mäkelä, 2019; Monteleoni et al., 2013). Supervised learning is a form of ML in which an algorithm is trained on a suite of example input-output pairs to generate a function that can be used for mapping new inputs to outputs of interest. ML algorithms can be trained on different sets of inputs, also called features, and the resulting algorithm can be tested on out-of-sample data for evaluation. In this way, the relative importance of different features for predicting outputs can be quantified. In this study, we apply ML techniques to measurements and simulations of water vapor isotopic composition and conventional meteorological datasets from the SE Pacific marine stratocumulus region to estimate shallow convective moistening of the LFT.

Using observations from the SE Pacific, we will explore the links between in-situ isotopic measurements from the Chajnantor Plateau in northern Chile and the suite of features that will be analyzed in the ML component of the study and use an isotope-enabled climate model (LMDZ5B) to explicitly determine the relationships between these features and the shallow convective moistening tendencies output from the model. We then train a supervised ML algorithm with conventional as well as isotopic fields from LMDZ5B simulations to determine the utility of isotopic fields for estimating shallow convective moistening. The ML will be trained on 3 years of model output from an Atmospheric Model Intercomparison Project (AMIP) simulation and tested on 2 years of out-of-sample AMIP output. An ongoing issue in the application of ML to climate modeling is the generalizability of a trained ML algorithm to different climates. We explore this issue in the context of stable isotopes by extending the analysis to include preindustrial (PI) and quadrupled CO2 (4X) simulations. We will demonstrate that stable isotopes in water vapor do indeed offer important benefits for estimating shallow convective moistening. We then apply the ML algorithm that was trained on GCM output to the observations from the SE Pacific to generate observationally-constrained estimates of shallow convective moistening tendencies. The ability to estimate these tendencies from isotopic and other observations may provide a useful link between observations and models for evaluating the processes governing marine low-cloud variability.

## 3 Methods

A comprehensive review of the analysis of stable isotopes in atmospheric water vapor is provided in Galewsky et al. (2016). We use in-situ measurements of water vapor mixing ratio and isotopic composition acquired at an elevation of 5 km at the Atacama Large Millimeter (ALMA) Observatory, on the Chajnantor Plateau in northern Chile (Figure 1), between 13 July, 2014, and 12 August, 2017 using a Picarro L2130 cavity ring-down spectroscopy (CRDS) analyzer. Galewsky (2018a) showed that the in-situ measurements at this site are coherently linked to offshore inversion strength and cloud cover. We estimate the 1-$\sigma$ uncertainties in the measurements reported here to be 2.5‰ in $\delta$D. The humidity measurements from the L2130 were compared to other meteorological instruments on the Chajnantor Plateau (not shown) and no systematic bias in humidity measurements was observed. Winds at Chajnantor are predominantly from the west-northwest, but about 10% of the data were associated with easterly winds, primarily during the South American monsoon. Such periods are not directly influenced by the processes over the southeast Pacific that are the focus of the current study and are omitted from this analysis. A full description of this dataset is presented in Galewsky (2018a) and the citations therein.

As described in previous studies (Galewsky, 2018a, 2018b) the difference, in permil, between an isotopic measurement at a given mixing ratio and the $\delta$-value of the idealized Rayleigh distillation process to the same mixing ratio is a useful metric that can be interpreted in terms of moistening processes. This quantity will be referred to here as $\Delta\delta$D, and its utility in the estimation of shallow convective moistening tendencies will be quantitatively evaluated here. This metric is similar to the $\delta D_q$ used by Bailey et al. (2017). A high value of $\Delta\delta$D is usually associated with a small degree of moistening of a dry, isotopically-depleted airmass by a moist, isotopically-enriched airmass, while low values of $\Delta\delta$D are associated with greater moistening. For the observations, $\Delta\delta$D is computed using the temperature profile from the daily soundings for the Rayleigh distillation calculation, and for the GCM output, it is computed using daily average temperature profiles over the region shown in Figure 1.

Following Galewsky (2018b) and Galewsky (2018a), the strength of the inversion was estimated in terms of the Estimated Inversion Strength (EIS, (Wood & Bretherton, 2006)) which is given by: $EIS = LTS - \Gamma_m^{850}(z_{700} - LCL)$, where LTS is the lower-tropospheric stability (defined as $LTS = \theta_{700hPa} - \theta_{surface}$), $\Gamma$ is a moist adiabat at 850 hPa, $z_{700}$ is the height of the 700 hPa surface, and the LCL is the lifting condensation level. EIS was computed from the daily soundings (noon UTC) at Antofagasta using the method of Wood and Bretherton (2006). The time series of EIS was interpolated to coincide with the 12-hour averaged isotopic data from Chajnantor. Daily mean cloud fraction was retrieved from the Aqua Atmosphere Level 3 Daily Joint Aerosol/Water Vapor/Cloud product (Platnick et al., 2003) from the region over the SE Pacific shown in Figure 1 and are compared with daily averages of EIS. Daily SST data from the region is obtained from the NOAA High Resolution Blended Analysis of Daily SST (Reynolds et al., 2007).

Relative humidity (RH) profiles are derived from the SAPHIR sounder on the Megha-Tropiques satellite (Brogniez et al., 2016; Sivira et al., 2015). The satellite samples a given point between 3 and 5 times daily, and here we use daily averages of the operational Level 2 RH product gridded at a $1° \times 1°$ resolution, in which we retain data with at least 95% valid RH values within each gridbox. Atmospheric RH is determined for multiple pressure layers, and here we focus on the RH in the 850 hPa to 1000 hPa layer, the 700 hPa to 500 hPa layer, and the difference between the two layers ($\Delta$RH). The SAPHIR RH is useful as an independent measure of humidity because the retrieval does not rely on a priori assumptions about temperature profiles or integrated water vapor content.

For the AMIP simulations, we use nudged 2007-2011 simulations computed by LMDZ5B (Hourdin et al., 2013), the most recent isotopically-enabled version of this GCM. Stable isotopologues of water are implemented in this version in a way similar to LMDZ4 (Risi et al., 2010) and other state-of-the-art isotope-enabled GCMs. LMDZ5B is run here with 96 points in longitude (3.75° resolution at Equator), 72 points in latitude (2.5° resolution) and 39 vertical levels (over the oceans, the lowest 5 levels span the surface to 500m). LMDZ5B is forced by monthly-mean sea surface conditions (SST and sea ice) following the AMIP protocol (Gates, 1992). Horizontal winds are nudged towards ERA-40 reanalyses (Uppala et al., 2005) to ensure a more realistic simulation. We use 5 years (2007-2011) of a simulation that was initialized in 1977 (Risi et al., 2010). For the PI simulations, the sea surface conditions come from the pre-industrial simulation run by the IPSL-CM5A-MR coupled model (Dufresne et al., 2013) as part of the CMIP5 exercise (Taylor et al., 2012). The last 30 years of the coupled simulation is used to calculate multi-year-averages of monthly-mean sea surface conditions. LMDZ5B is run with atmospheric forcing conditions similar to the pre-industrial simulation imposed by CMIP5. For example, the CO2 concentration is 280ppm. The simulation is initialized from a previously well-equilibrated simulation for present-day (Risi et al., 2010) and run for 15 years. The first 10 years of simulation are discarded for spin-up and the last 5 years are analyzed. For the 4xCO2 simulation, LMDZ5B is forced by sea surface conditions coming from the last 30 years of an abrupt 4x CO2 simulation with IPSL-CM5A-MR as part of the CMIP5 exercise. Atmospheric conditions are the same as in the PI simulation except that CO2 concentrations are quadrupled.

In this study, the GCM output is averaged over the SE Pacific marine stratocumulus region as shown in Figure 1. The averaging region covers the highest average simulated LCF in the SE Pacific and exhibits large day-to-day variability, making it suitable for analyzing the processes governing variability in LCF. Experiments with different averaging regions (not shown) yielded very similar results, although other regions with less day-to-day variability in cloud fraction were found to yield less realistic results when applied to the observations from Chajnantor. We focus on the SE Pacific region because of the opportunity to use the in-situ measurements from Chajnantor. Future studies will extend this analysis to other marine low-cloud regions using satellite remote sensing of water vapor isotopologues.

Within LMDZ, there is very little difference between the low-cloud fraction and the total cloud fraction in the averaging region, and GPR models that were trained on the total cloud fraction yielded nearly identical results to the models trained on the low-cloud fractions. In observations from Aqua, 95% of the retrieved cloud-top pressures are above 650 hPa, and more than 70% are above 800 hPa. Given the dominance of the total cloud fraction by low clouds in the SE Pacific marine stratocumulus region, comparisons between GCM output and observations in this application are relatively straightforward.

LMDZ5B has several important advances in model physics over earlier versions. Most relevant for this study is that LMDZ5B has separate parameterizations for shallow convection, which is handled by the thermal plume model of Rio and Hourdin (2008), and deep convection, which is handled by the scheme of Emanuel (1991). In addition, LMDZ5B implemented for the first time a parameterization of cold pools generated below cumulonimbus whose spreading can trigger additional convection (Grandpeix & Lafore, 2010). LMDZ5B has a self-described 'kludge' (Hourdin et al., 2013, 2019, 2020), important in marine low-cloud regions, in which the thermal plume model is turned off if there is a sharp temperature inversion at the top of the boundary layer. In practice, shallow convective moistening in LMDZ5B may be effected by the thermal plume model, the Emanuel convection scheme, the cold pool scheme, or by a combination of the three, depending on the meteorological conditions. Here, we interpret the sum of these three moistening tendencies at the 830 hPa level as a total shallow convective moistening tendency.

The machine learning algorithm used here is a Gaussian process regression model (GPR, Rasmussen and Williams (2006)). GPR models are nonparametric, kernel-based, probabilistic supervised learning models. While there are many similar ML algorithms, we chose the GPR because it yielded good results in terms of RMS errors and good performance in terms of computational time. We explore a range of input features, including $\delta$D, $\Delta\delta D$, EIS, SST, mixing ratio, cloud fractions, and relative humidity, and quantitatively evaluate the resulting GPR models against out-of-sample GCM output. We seek parsimonious models, which are models that make accurate predictions with as few predictor variables as possible.

# 4 Results

## 4.1 In-situ measurements from Chajnantor and remote sensing of cloud and humidity

Previous studies have shown how EIS and SST control cloud fractions in marine stratocumulus regions (Qu et al., 2014), and these parameters are also closely associated with stable isotopes and mixing ratios in the LFT. Figure 2A and B shows the the relationships between mixing ratio and $\delta$D from Chajnantor and how they relate to inversion strength (Fig. 2A) and SST (Fig. 2B). There is an inverse relationship of EIS with mixing ratio and $\delta$D, and a positive relationship of SST with mixing ratio and $\delta$D. Galewsky (2018a) previously interpreted this dataset in terms of EIS, but did not consider SST. The smallest cloud fractions are associated with high $\delta$D values and low values of $\Delta\delta$D (Figure 2C) while large low-cloud fractions are associated with a broad range of $\delta$D values ($-400$‰ to $-100$‰) and high $\Delta\delta$D. The lowest decile of cloud fraction is 0.57, and the range of $\delta$D values corresponding to cloud fractions below 0.57 is 251‰, while the total range of $\delta$D measurements from Chajnantor is 367‰. The $\delta$D measurements corresponding to the lowest decile of cloud fractions thus span 69% of the total range of $\delta$D measurements from Chajnantor. The relationships between cloud fraction and the total water vapor mixing ratio are more scattered (Figure 2D) than the relationships between cloud fraction and $\delta$D . While large cloud fractions and high $\Delta\delta$D are consistently associated with low mixing ratios, the mixing ratios corresponding to the lowest decile of cloud fraction spans 85% of the total range of mixing ratios measured at Chajnantor.

Figure 3 shows the relationships between $\delta$D, cloud fractions, and SAPHIR RH in the MBL (850 hPa to 1000 hPa), aloft (500 hPa - 700 hPa), and the RH gradient (the difference between the RH at those two levels). High $\delta$D in the LFT is associated with the lowest MBL RH and the smallest cloud fractions (Fig. 3A). For the lowest decile of cloud fractions, the MBL RH averages 80%, while for the highest decile of cloud fractions it averages 88%. Aloft (Fig. 3B), the record is more scattered, with high $\delta$D and small cloud fractions associated with slightly elevated RH (average RH of 17% for the lowest decile of cloud fractions and RH of 14% for the highest decile of cloud fractions). The difference between the RH in the MBL and the RH aloft ($\Delta$RH) is shown in (Fig. 3C). For the lowest decile of cloud fractions, $\Delta$RH=63% while for the highest decile, $\Delta$RH=74%.

The observational data are consistent with the transport of moist, isotopically-enriched air from the MBL into the LFT when EIS is low and SST is high. Under these conditions, the RH in the MBL is reduced while the RH aloft increases, and the cloudy layer, deprived of water vapor, experiences reduced cloud fractions. We hypothesize that shallow convective moistening of the LFT is at the heart of these relationships, and that the high water vapor $\delta$D values measured under low EIS/high SST conditions reflect the effects of shallow convection in transporting isotopically enriched water vapor from the MBL into the LFT.

### 4.2 GCM Simulations

Figure 4 shows some of the main results from five-year (2007-2011) averages of the LMDZ5B AMIP simulation at 830 hPa for the marine stratocumulus region shown in Figure 1. The maximum cloud fraction is within the boundary layer, typically at around

950 hPa (not shown), and the top of the inversion, when present, is at around 900 hPa. Thus, our analysis at 830 hPa is in the lower free troposphere, above the MBL. Figures 4A and B show how the simulated 830 hPa mixing ratios and $\delta$D respond to EIS and SST. As expected, there is to first-order an inverse relationship of EIS with mixing ratio and $\delta$D (Fig. 4A) and a positive relationship between these fields and SST (Fig. 4B). There are two maxima in the water vapor $\delta$D values. One is associated with the highest mixing ratios, lowest EIS, and highest SST and occurs during summer, while the other maximum is associated with drier conditions, higher EIS, and lower SST, and occurs during winter. The maxima likely reflect the reorganization of water vapor transport pathways between the summer monsoon and the more zonal wintertime circulation (Galewsky & Samuels-Crow, 2015). The smallest low-cloud fractions are associated with a narrow band of high $\delta$D and low $\Delta\delta$D (Fig. 4C), while the smallest low-cloud fractions are associated with a more scattered band of elevated mixing ratio (Fig. 4D).

The range of relative humidity in the lowest model level is narrow (Fig. 5A), but the smallest cloud fractions are associated with lower RH and the highest $\delta$D values. Aloft, there is much greater range (Fig. 5B) in RH, with a clear relationship between larger 830 hPa RH, larger $\delta$D values, and smaller cloud fractions. Finally, a reduction (or vanishing) of the difference in RH between the two levels is clearly associated with larger $\delta$D and smaller cloud fractions.

Thus far, the relationships shown from the GCM are similar to, if much less scattered than, the same sets of relationships we saw from the observations. A link between these relationships and the transport of water vapor from the MBL into the LTS is certainly in line with our expectations, but now, using the GCM output, we can directly investigate this process by analyzing the shallow convective moistening tendencies. Scatterplots of the relationships between $\delta$D and shallow convective moistening tendencies (Figure 6A) are skewed, with the highest $\delta$-values associated with low RH gradients and high moistening tendencies. In contrast, the relationships between mixing ratio and shallow convective moistening tendencies exhibit larger scatter, with maxima in dq/dt occurring at intermediate mixing ratios, further illustrating that $\delta$D responds differently to shallow convective moistening than mixing ratio. Along the same lines, Figure 7A shows how the smallest low-cloud fractions are associated with the highest $\delta$D and dq/dt values, with more scatter in the relationships between dq/dt and cloud fraction with mixing ratio (Fig. 7B). Small low-cloud fractions are also associated with elevated values of dq/dt and small values of $\Delta\delta$D (Figure 7C).

The suite of relationships described here are consistent with the nonlinear mixing between dry, isotopically depleted air masses and moist, isotopically enriched air masses (Galewsky and Hurley (2010), Bailey et al. (2017), and see Figure 1 in Galewsky (2018b)). A dry, isotopically depleted airmass lowers the mixing ratio of a moist airmass more than it isotopically depletes it, which means that the isotopic composition of a moisture source derived from the MBL will be largely preserved even as that source mixes with dry, isotopically-depleted air from the LFT. It is this preservation of the isotopic composition of MBL water vapor in the LFT that allows us to quantitatively diagnose moistening from isotopic observations in the LFT.

### 4.3 GPR modeling of AMIP simulation

In the previous sections, we demonstrated how water vapor isotopic composition in the LFT over the SE Pacific marine stratocumulus region responds to shallow convective moistening tendencies. Now we use a machine learning technique to gain further insight into the potential utility of water vapor isotopic composition for estimating shallow convective moistening tendencies. We train the GPR algorithm using three years of the AMIP simulation (2007-2009) and use the remaining two years (2010-2011) for out-of-sample evaluation of the algorithm.

A key step in supervised learning algorithms is the selection of the input data (features). While there is wide latitude in the selection of features, we focused on features that readily translate into field or remote sensing observations. We focused on different combinations of EIS, SST, LCF, $\delta$D, $\Delta\delta$D, q, and RH. The outputs are the shallow convective moistening tendencies at 830 hPa. The training dataset was the time series of GCM output averaged over the SE Pacific marine stratocumulus region shown in Figure 1.

For cross-validation, the training data was divided into 5 disjoint folds. For each fold, the model was trained on out-of-fold data and was assessed using in-fold data. The average test error over all of the folds was used to assess the model. Once the best-fitting model was determined using the 2007-2009 GCM output, it was applied to the output from 2010-2011 for the out-of-sample results presented in Table 1.

The results shown in Table 1 show that there is remarkable predictive value in the use of isotopic fields. The combination of EIS, $\delta$D, $\Delta\delta$D, and q (the EIS_ISO model) provide very nearly the same quality of fit as those same fields supplemented with relative humidity at the surface and at 830 hPa ($RH_{surf}$, $RH_{LFT}$, respectively), SST, and LCF (the FULL_ISO model). The best-fitting model that uses only non-isotopic fields (EIS, $RH_{surf}$, $RH_{LFT}$, q, SST, LCF; the NO_ISO model) is less parsimonious than the EIS_ISO model and has metrics that are less favorable than most of the models that use isotopic fields. Figure 8 shows scatterplots of the estimates of 830 hPa dq/dt from (A) the EIS_ISO model and (B) the NO_ISO model and (C) the FULL_ISO models compared to the GCM output. The slope of the best-fitting line in EIS_ISO is 0.9, while the slopes of the best-fitting lines in NO_ISO and FULL_ISO are 0.70 and 0.76, respectively.

The time series of the 830 hPa shallow convective moistening tendency from the GCM is superimposed on the time series derived from the FULL_ISO GPR model in Figure 9 for the out-of-sample years 2010-2011. The GPR model clearly captures the seasonal variability in dq/dt and matches most of the variability on shorter time-scales as well. The GPR model also captures the main relationships between dq/dt, EIS, $\delta$D, $\Delta$RH, $\delta$D, $q$, and cloud fraction (not shown)

### 4.4 Generalization to Different Climates

An important question in ML studies of climate models is the extent to which the ML algorithm trained in one climate works in another climate, either warmer or cooler. We first explore how well the GPR model trained on AMIP output predicts the shallow convective dq/dt in the LMDZ5B preindustrial simulation (PI) and the quadrupled CO2 simulations (4X). In neither case is the performance very good (see Table 2 for details), although the FULL_ISO model applied to the PI simulation yields the best performance with RMS error of 0.347 and an $R^2$ of 0.686. The AMIP-trained models are especially poor at estimating the shallow convective dq/dt for the quadrupled CO2 simulation, with the EIS_ISO simulation coming in with a remarkably low $R^2$ of 0.002, and the other results displaying very large negative biases in the estimates of dq/dt.

This result is in line with O'Gorman and Dwyer (2018), who showed that ML algorithms trained in one climate may perform reasonably well in a cooler climate, but quite poorly in a warmer climate. Their study showed that a given latitude within a cooler climate may be predicted by a higher latitude within a warmer climate, but not vice-versa. They also showed that training an ML algorithm on features from multiple climates can yield better results than training on a single climate state. We trained the GPR algorithms on 3 years each from the PI and 4X CO2 simulations, and then applied it to the two out-of-sample years for each, as well as the 2010-2011 AMIP simulations. These results are summarized in Table 2. The models trained only on the quadrupled CO2 simulation do better in the cooler climates (AMIP and PI) than the AMIP-trained models did on the 4X CO2 simulation, but in neither case are the results very good. The models trained on the 4X simulations do very well for the out-of-sample years in the 4X simulations, with the FULL_ISO model performing better than either EIS_ISO or NO_ISO models, indicating the value of water vapor $\delta$D in the LFT for estimating shallow convective moistening in the warmer climate. The blended models that were trained on both PI and 4X simulations do very well on the out-of-sample PI and 4X years, with the FULL_ISO model yielding the best results. The blended models are less successful on the AMIP climate, probably because the PI and 4X simulations share systematic SST biases that are not present in AMIP, but nevertheless yield better results than the models trained exclusively on the 4X simulation.

When evaluating these climate change simulations, it is the differences in dq/dt between PI and 4X that are of particular importance, rather than the absolute values for either climate state. The average difference in dq/dt as simulated by the GCM (4X-PI) is -0.166 g/kg/day, and the average difference as simulated by the blended FULL_ISO GPR is -0.150 g/kg/day, or a difference of about 10%. Given the complexity of the physical processes that are involved, these results suggest that the use of isotopic fields in conjunction with machine learning algorithms may be a promising avenue for evaluating changes in shallow convective moistening in a changing climate.

### 4.5 Application to Observations

The GPR models described above were broadly successful in reproducing GCM shallow convective moistening tendencies in the lower free troposphere given a relatively simple input dataset of easily measurable quantities. These quantities are all readily available from the Chajnantor dataset described earlier, suggesting the possibility of using a GCM-trained algorithm to estimate dq/dt from observations. Given the challenges of estimating mixing process from observations (Lamer et al., 2015; Vogel et al., 2020), an isotopically-based method for estimating moistening tendencies may be useful as a complementary approach to other methods.

We computed dq/dt using the FULL_ISO model, and the time series is shown in Figure 10. The estimated dq/dt range from zero up to just over 1.5 g/kg/day and shows the expected seasonal cycle in dq/dt, with higher dq/dt during Austral summer. The $1-\sigma$ uncertainties vary with the estimated dq/dt, ranging from around 0.6 g/kg/day for the highest values of dq/dt, and up to more than 1 g/kg/day for the lowest values of dq/dt. It is possible that larger training datasets may sample a broader range of conditions and could lower the estimated uncertainties, and future studies will focus on how to reduce these uncertainties.

Figure 11 shows the relationships between measured $\delta$D, mixing ratio, $\Delta\delta$D and cloud fractions with the estimated dq/dt from the GPR. The GPR generates relationships that are consistent with the GCM results, with higher dq/dt associated with higher $\delta$D and smaller cloud fractions (Fig. 11A), and larger scatter between dq/dt and mixing ratios (Fig. 11B). The smallest cloud fractions are associated with higher dq/dt than the largest cloud fractions, and area associated with smaller $\Delta\delta$D (Fig. 11C). Similar results are obtained for the relationships between dq/dt, $\delta$D, and RH (Fig. 12), with high values of dq/dt associated with small values of $\Delta$RH.

Finally, we can use the output of this GPR model to estimate how EIS modulates shallow convective moistening based on the Chajnantor dataset (Figure 13). While there is quite a bit of scatter in the results, there is a negative relationship between EIS and dq/dt and between dq/dt and cloud fraction. For the lowest quartile of EIS, corresponding to EIS below 10.5K, the GPR estimates the average shallow convective dq/dt to be 0.58 g/kg/day, while for the highest quartile of EIS, corresponding to EIS above 14.5K, the GPR estimates shallow convective dq/dt to be 0.29 g/kg/day.

## 5 Discussion

There have been a number of studies that have attempted to quantify convective moistening tendencies, including indirect approaches using models (Hohenegger & Stevens, 2013), sounding networks (Schumacher et al., 2008), or satellites (Masunaga, 2013). Bellenger et al. (2015) used a variety of observations collected during the Cooperative Indian Ocean Experiment on Intraseasonal Variability/ Dynamics of the MJO (CINDY/DYNAMO) campaign to directly estimate shallow convective moistening tendencies across a range of time scales. On time scales of a few minutes, they identified moistening tendencies of 10-20 g/kg/day, while on time scales of several hours, the moistening tendencies were 1-4 g/kg/day. Our estimates of shallow convective moistening tendencies based on the isotopic observations from Chajnantor are 0-1.5 g/kg/day, which are consistent with the longer time-scales of Bellenger et al. (2015) and the studies cited therein. Furthermore, the approach used by Bellenger et al. (2015) could potentially be complemented by isotopic measurements to build a machine learning algorithm for estimating dq/dt based entirely on observations.

One of the most striking outcomes of this analysis is the extent to which the use of isotopic fields improves GPR estimates of dq/dt. There has been a vigorous debate in recent years about the utility of isotopic measurements for providing additional information about the atmospheric hydrologic cycle beyond measurements of total mixing ratio (Risi et al., 2019; Duan et al., 2018), and the present analysis demonstrates the value of such measurements for estimating shallow convective moistening in a marine stratocumulus setting. The application of the GPR model to observations yielded physically consistent results, but any biases in the GCM's relationship between convective moistening and the input variables will be mapped onto any GCM-trained algorithm for estimating dq/dt from observations. In principle, there should be no problem extending this analysis to other marine low-cloud regions, and one could potentially train a GPR with the model output from all marine low-cloud regions. Remote sensing datasets of water vapor isotopic composition could provide the necessary observational inputs, but the uncertainties in remote sensing datasets are larger than the in-situ measurements used here, and the suitability of such datasets for this application will require further analysis that is well beyond the scope of the present study. It would also be interesting to apply this isotope-enabled ML approach to output from an isotope-enabled cloud-resolving model or large-eddy simulations of marine stratocumulus clouds, as this is the approach used in studies seeking to improve convective parameterizations (O'Gorman & Dwyer, 2018; Gentine et al., 2018). The use of isotopic measurements and simulations with ML techniques may provide an avenue for improved ML-based parameterizations of shallow convection.

The studies of Galewsky (2018b, 2018a) used an inverse modeling approach to partition the joint distribution of mixing ratio and isotopic composition into two reservoirs, a dry, isotopically-depleted airmass associated with a last-saturation temperature in the upper troposphere, and a moist, isotopically-enriched airmass associated with an MBL moistening source. This technique provided internally consistent results that were statistically indistinguishable from the observations, but extensive testing of this framework with GCM output (not shown) failed to yield results that consistently scaled with convective moistening tendencies in out-of-sample testing. The processes governing the joint distribution of mixing ratio and isotopic composition are highly non-unique, and the additional constraints used here with the GPR algorithm yielded much more reliable results.

Finally, the model used here, LMDZ5B, does indeed show expected relationships between changes in EIS, LCF, and lower-tropospheric moistening, but we must note that this response is partially hard-wired into the model. As outlined by Hourdin et al. (2013), this version of the model is set to turn off the thermal plume model if there is a sharp temperature inversion at the top of the planetary boundary layer, although shallow convective moistening may still be effected by the Emanuel convection and cold pool wake schemes even when the thermal plume model is deactivated. It remains to be seen if a model with free-running shallow convection would yield similar results. We will be able to test this when an isotope-enabled version of LMDZ6 is available (Hourdin et al., 2019, 2020).

## 6 Conclusions

We have investigated how a GPR algorithm applied to shallow convective moistening tendencies in the SE Pacific marine stratocumulus region behaves when trained with the stable isotopic composition of water vapor in addition to more routine meteorological fields. Encouragingly, the use of isotopic fields was found to lead to parsimonious, robust, and accurate estimates of shallow convective moistening tendencies in AMIP simulations with better metrics than GPR algorithms trained without the isotopic fields. Climate change was accurately simulated only when training data from both a cool and warm climate were used. When applied to isotopic and conventional measurements from the SE Pacific region, the GPR trained on the AMIP simulations yielded physically realistic estimates of shallow convective moistening tendencies that showed the expected inverse relationship with EIS.

The setting we have used here is restricted to the SE Pacific and to a relatively coarse GCM with conventional convective parameterizations. It would be interesting to extend this study to include training of the GPR across other marine stratocumulus settings, possibly using satellite remote sensing of isotopic fields as part of the training dataset. It would also be interesting to apply similar machine learning approaches to simulations of resolved convection in cloud-resolving models or large-eddy simulations. When combined with intensive isotopic and conventional measurements, such as were obtained in the EUREC4A field campaign (Bony et al., 2017), such an approach may yield useful, independent constraints on shallow convection and, ultimately, better understanding of low-cloud feedbacks.

## Acknowledgments

This work was supported by the LABEX-IPSL visitor program, the Franco-American Fulbright Foundation, and NSF AGS Grants 1738075 and 1158582 to JG. The LMDZ simulation used the HPC resources of IDRIS under the allocation 2092 given by GENCI. We thank Sandrine Bony, Nicolas Rochetin, Frederic Hourdin, and Jean-Yves Grandpeix for helpful discussions. GCM output used in this analysis available at https://bit.ly/2x4QDWB. NOAA High Resolution SST data provided by the NOAA/OAR/ESRL PSD, Boulder, Colorado, USA, from their Web site at https://www.esrl.noaa.gov/psd/. The isotopic data used here is provided as supplemental data in the cited publications. We also thank the national Aeris data center that hosts the entire Megha-Tropiques data archive, freely available from the portal https://en.aeris-data.fr

## References

Bailey, A., Blossey, P. N., Noone, D., Nusbaumer, J., & Wood, R. (2017). Detecting shifts in tropical moisture imbalances with satellite-derived isotope ratios in water vapor. *Journal of Geophysical Research: Atmospheres*, *122*(11), 5763–5779. doi: 10.1002/2016jd026222

Bellenger, H., Yoneyama, K., Katsumata, M., Nishizawa, T., Yasunaga, K., & Shirooka, R. (2015). Observation of Moisture Tendencies Related to Shallow Convection. *Journal of the Atmospheric Sciences*, *72*(2), 641–659. doi: 10.1175/jas-d-14-0042.1

Bony, S., & Dufresne, J. L. (2005). Marine boundary layer clouds at the heart of tropical cloud feedback uncertainties in climate models. *Geophysical Research Letters*, *32*(20). doi: 10.1029/2005gl023851

Bony, S., Dufresne, J. L., Treut, H. L., Morcrette, J. J., & Senior, C. (2004). On dynamic and thermodynamic components of cloud changes. *Climate Dynamics*, *22*(2-3), 71 86. doi: 10.1007/s00382-003-0369-6

Bony, S., Stevens, B., Ament, F., Bigorre, S., Chazette, P., Crewell, S., ... Wirth, M. (2017). EUREC¡Superscript¿4¡/Superscript¿A: A Field Campaign to Elucidate the Couplings Between Clouds, Convection and Circulation. *Surveys in Geophysics*, *38*(6), 1529 1568. doi: 10.1007/s10712-017-9428-0

Brenowitz, N. D., & Bretherton, C. S. (2018). Prognostic Validation of a Neural Network Unified Physics Parameterization. *Geophysical Research Letters*, *45*(12), 6289–6298. doi: 10.1029/2018gl078510

Brient, F., Schneider, T., Tan, Z., Bony, S., Qu, X., & Hall, A. (2016). Shallowness of tropical low clouds as a predictor of climate models' response to warming. *Climate Dynamics*, *47*(1-2), 433 449. doi: 10.1007/s00382-015-2846-0

Brogniez, H., Fallourd, R., Mallet, C., Sivira, R., & Dufour, C. (2016). Estimating Confidence Intervals around Relative Humidity Profiles from Satellite Observations: Application to the SAPHIR Sounder. *Journal of Atmospheric and Oceanic Technology*, *33*(5), 1005–1022. doi: 10.1175/jtech-d-15-0237.1

Chung, D., & Teixeira, J. (2012). A Simple Model for Stratocumulus to Shallow Cumulus Cloud Transitions. *Journal of Climate*, *25*(7), 2547 2554. doi: 10.1175/jcli-d-11-00105.1

Duan, S. Q., Wright, J. S., & Romps, D. M. (2018). On the Utility (or Futility) of Using Stable Water Isotopes to Constrain the Bulk Properties of Tropical Convection. *Journal of Advances in Modeling Earth Systems*, *10*(2), 516–529. doi: 10.1002/2017ms001074

Dufresne, J. L., Foujols, M.-A., Denvil, S., Caubel, A., Marti, O., Aumont, O., ... Vuichard, N. (2013). Climate change projections using the IPSL-CM5 Earth System Model: from CMIP3 to CMIP5. *Climate Dynamics*, *40*(9-10), 2123 2165. doi: 10.1007/s00382-012-1636-1

Dussen, J. J. v. d., Roode, S. R. d., Gesso, S. D., & Siebesma, A. P. (2015). An LES model study of the influence of the free tropospheric thermodynamic conditions on the stratocumulus response to a climate perturbation. *Journal of Advances in Modeling Earth Systems*, *7*(2), 670–691. doi: 10.1002/2014ms000380

Emanuel, K. A. (1991). A Scheme for Representing Cumulus Convection in Large-Scale Models. *Journal of the Atmospheric Sciences*, *48*(21), 2313 2335. doi: 10.1175/1520-0469(1991)048⟨2313:asfrcc⟩2.0.co;2

Galewsky, J. (2018a). Relationships Between Inversion Strength, Lower-Tropospheric Moistening, and Low-Cloud Fraction in the Subtropical Southeast Pacific Derived From Stable Isotopologues of Water Vapor. *Geophysical Research Letters*, *45*(15), 7701 7710. doi: 10.1029/2018gl078953

Galewsky, J. (2018b). Using Stable Isotopes in Water Vapor to Diagnose Relationships Between Lower-Tropospheric Stability, Mixing, and Low-Cloud Cover Near the Island of Hawaii. *Geophysical Research Letters*, *45*(1), 297 305. doi: 10.1002/2017gl075770

Galewsky, J., & Hurley, J. V. (2010). An advection-condensation model for subtropical water vapor isotopic ratios. *Journal of Geophysical Research: Atmospheres*, *115*(D16). Retrieved from `http://dx.doi.org/10.1029/2009JD013651` doi: 10.1029/2009jd013651

Galewsky, J., Larsen, H. C. S., Field, R. D., Worden, J., Risi, C., & Schneider, M. (2016). Stable isotopes in atmospheric water vapor and applications to the hydrologic cycle. *Reviews of Geophysics*, *54*(4). doi: 10.1002/2015rg000512

Galewsky, J., & Rabanus, D. (2016). A Stochastic Model for Diagnosing Subtropical Humidity Dynamics with Stable Isotopologues of Water Vapor. *Journal of the Atmospheric Sciences*, *73*(4), 1741 1753. doi: 10.1175/jas-d-15-0160.1

Galewsky, J., & Samuels-Crow, K. (2015). Summertime Moisture Transport to the Southern South American Altiplano: Constraints from In Situ Measurements of Water Vapor Isotopic Composition. *Journal of Climate*, *28*(7), 2635 2649. doi: 10.1175/jcli-d-14-00511.1

Gates, W. L. (1992). AMIP: The Atmospheric Model Intercomparison Project. *Bulletin of the American Meteorological Society*, *73*(12), 1962–1970. doi: 10.1175/1520-0477(1992)073⟨1962:atamip⟩2.0.co;2

Gentine, P., Pritchard, M., Rasp, S., Reinaudi, G., & Yacalis, G. (2018). Could Machine Learning Break the Convection Parameterization Deadlock? *Geophysical Research Letters*, *45*(11), 5742–5751. doi: 10.1029/2018gl078202

Grandpeix, J.-Y., & Lafore, J.-P. (2010). A Density Current Parameterization Coupled with Emanuel's Convection Scheme. Part I: The Models. *Journal of the Atmospheric Sciences*, *67*(4), 881 897. doi: 10.1175/2009jas3044.1

Hohenegger, C., & Stevens, B. (2013). Preconditioning Deep Convection with Cumulus Congestus. *Journal of the Atmospheric Sciences*, *70*(2), 448–464. doi: 10.1175/jas-d-12-089.1

Hourdin, F., Grandpeix, J.-Y., Rio, C., Bony, S., Jam, A., Cheruy, F., ... Roehrig, R. (2013). LMDZ5B: the atmospheric component of the IPSL climate model with revisited parameterizations for clouds and convection. *Climate Dynamics*, *40*(9-10), 2193 2222. doi: 10.1007/s00382-012-1343-y

Hourdin, F., Jam, A., Rio, C., Couvreux, F., Sandu, I., Lefebvre, M., ... Idelkadi, A. (2019). Unified Parameterization of Convective Boundary Layer Transport and Clouds With the Thermal Plume Model. *Journal of Advances in Modeling Earth Systems*. doi: 10.1029/2019ms001666

Hourdin, F., Rio, C., Grandpeix, J., Madeleine, J., Cheruy, F., Rochetin, N., ... Ghattas, J. (2020). LMDZ6A: the atmospheric component of the IPSL climate model with improved and better tuned physics. *Journal of Advances in Modeling Earth Systems*, e2019MS001892. doi: 10.1029/2019ms001892

Lamer, K., Kollias, P., & Nuijens, L. (2015). Observations of the variability of shallow trade wind cumulus cloudiness and mass flux: OBSERVATION OF SHALLOW TRADE WIND CUMULI. *Journal of Geophysical Research: Atmospheres*, *120*(12), 6161–6178. doi: 10.1002/2014jd022950

Masunaga, H. (2013). A Satellite Study of Tropical Moist Convection and Environmental Variability: A Moisture and Thermal Budget Analysis. *Journal of the Atmospheric Sciences*, *70*(8), 2443–2466. doi: 10.1175/jas-d-12-0273.1

Monteleoni, C., Schmidt, G. A., & McQuade, S. (2013). Climate Informatics: Accelerating Discovering in Climate Science with Machine Learning. *Computing in Science & Engineering*, *15*(5), 32–40. doi: 10.1109/mcse.2013.50

O'Gorman, P. A., & Dwyer, J. G. (2018). Using machine learning to parameterize moist convection: potential for modeling of climate, climate change and extreme events. *Journal of Advances in Modeling Earth Systems*, *10*(10), 2548–2563. doi: 10.1029/2018ms001351

Platnick, S., King, M. D., Ackerman, S. A., Menzel, W. P., Baum, B. A., Riedi,

J. C., & Frey, R. A. (2003). The MODIS cloud products: Algorithms and examples from Terra. *Geoscience and Remote Sensing, IEEE Transactions on*, *41*(2), 459 473. doi: 10.1109/tgrs.2002.808301

Qu, X., Hall, A., Klein, S. A., & Caldwell, P. M. (2014). On the spread of changes in marine low cloud cover in climate model simulations of the 21st century. *Climate Dynamics*, *42*(9-10), 2603 2626. doi: 10.1007/s00382-013-1945-z

Rasmussen, C., & Williams, C. (2006). *Gaussian Processes for Machine Learning.* MIT Press.

Reynolds, R. W., Smith, T. M., Liu, C., Chelton, D. B., Casey, K. S., & Schlax, M. G. (2007). Daily High-Resolution-Blended Analyses for Sea Surface Temperature. *Journal of Climate*, *20*(22), 5473–5496. doi: 10.1175/2007jcli1824.1

Rieck, M., Nuijens, L., & Stevens, B. (2012). Marine Boundary Layer Cloud Feedbacks in a Constant Relative Humidity Atmosphere. *Journal of the Atmospheric Sciences*, *69*(8), 2538 2550. doi: 10.1175/jas-d-11-0203.1

Rio, C., & Hourdin, F. (2008). A thermal plume model for the convective boundary layer: Representation of cumulus clouds. *Journal of the Atmospheric Sciences*, *65*(2), 407 425. doi: 10.1175/2007jas2256.1

Risi, C., Bony, S., Vimeux, F., & Jouzel, J. (2010). Water-stable isotopes in the LMDZ4 general circulation model: Model evaluation for present-day and past climates and applications to climatic interpretations of tropical isotopic records. *Journal of Geophysical Research: Atmospheres*, *115*(D12), D12118. doi: 10.1029/2009jd013255

Risi, C., Galewsky, J., Reverdin, G., & Brient, F. (2019). Controls on the water vapor isotopic composition near the surface of tropical oceans and role of boundary layer mixing processes. *Atmospheric Chemistry and Physics*, *19*(19), 12235–12260. doi: 10.5194/acp-19-12235-2019

Schumacher, C., Ciesielski, P. E., & Zhang, M. H. (2008). Tropical Cloud Heating Profiles: Analysis from KWAJEX. *Monthly Weather Review*, *136*(11), 4289–4300. doi: 10.1175/2008mwr2275.1

Sherwood, S. C., Bony, S., & Dufresne, J.-L. (2014). Spread in model climate sensitivity traced to atmospheric convective mixing. *Nature*, *505*(7481), 37–42. doi: 10.1038/nature12829

Sivira, R. G., Brogniez, H., Mallet, C., & Oussar, Y. (2015). A layer-averaged relative humidity profile retrieval for microwave observations: design and results for the Megha-Tropiques payload. *Atmospheric Measurement Techniques*, *8*(3), 1055–1071. doi: 10.5194/amt-8-1055-2015

Taylor, K. E., Stouffer, R. J., & Meehl, G. A. (2012). An Overview of Cmip5 and the Experiment Design. *Bulletin Of The American Meteorological Society*, *93*(4), 485 498. doi: 10.1175/bams-d-11-00094.1

Ukkonen, P., & Mäkelä, A. (2019). Evaluation of Machine Learning Classifiers for Predicting Deep Convection. *Journal of Advances in Modeling Earth Systems*, *11*(6), 1784–1802. doi: 10.1029/2018ms001561

Uppala, S. M., Kallberg, P. W., Simmons, A. J., Andrae, U., Bechtold, V. D. C., Fiorino, M., ... Woollen, J. (2005). The ERA-40 re-analysis. *Quarterly Journal of the Royal Meteorological Society*, *131*(612), 2961–3012. doi: 10.1256/qj.04.176

Vogel, R., Bony, S., & Stevens, B. (2020). Estimating the Shallow Convective Mass Flux from the Subcloud-Layer Mass Budget. *Journal of the Atmospheric Sciences*, *77*(5), 1559–1574. doi: 10.1175/jas-d-19-0135.1

Wood, R., & Bretherton, C. S. (2006). On the Relationship between Stratiform Low Cloud Cover and Lower-Tropospheric Stability. *Journal of Climate*, *19*(24), 6425 6432. doi: 10.1175/jcli3988.1

Zhang, M., Bretherton, C. S., Blossey, P. N., Austin, P. H., Bacmeister, J. T., Bony, S., ... Zhao, M. (2013). CGILS: Results from the first phase of an international project to understand the physical mechanisms of low cloud feedbacks in single column models. *Journal of Advances in Modeling Earth Systems*, *5*(4), 826 842. doi: 10.1002/2013ms000246

| **Features** | **RMSE** | **Adjusted $\mathbf{R^2}$** | **R** |
|---|---|---|---|
| EIS+q | 0.486 | 0.265 | 0.52 |
| EIS | 0.477 | 0.292 | 0.54 |
| $\delta$D+q | 0.459 | 0.346 | 0.59 |
| EIS+$\delta$D | 0.426 | 0.435 | 0.66 |
| EIS+$\delta$D+$\Delta\delta$D | 0.426 | 0.424 | 0.66 |
| $\delta$D+$\Delta\delta$D | 0.42 | 0.452 | 0.68 |
| EIS+$\delta$D+q | 0.412 | 0.471 | 0.69 |
| **EIS+$\mathbf{rh_{surf}}$+$\mathbf{rh_{ft}}$+q+SST+LCF** ***(NO_ISO Model)*** | 0.31 | 0.701 | 0.84 |
| EIS+$rh_{surf}$+$\delta$D+$\Delta\delta$D+q | 0.301 | 0.719 | 0.85 |
| EIS+SST+$\delta$D+$\Delta\delta$D+q | 0.299 | 0.722 | 0.85 |
| EIS+$rh_{surf}$+$rh_{ft}$+$\delta$D+$\Delta\delta$D+q+LCF | 0.297 | 0.726 | 0.86 |
| EIS+$rh_{surf}$+$rh_{ft}$+$\delta$D+$\Delta\delta$D+q | 0.293 | 0.733 | 0.86 |
| EIS+$rh_{ft}$+$\delta$D+$\Delta\delta$D+q | 0.29 | 0.739 | 0.86 |
| $\delta$D+q+$\Delta\delta$D | 0.284 | 0.749 | 0.87 |
| EIS+LCF+$\delta$D+$\Delta\delta$D+q | 0.282 | 0.752 | 0.87 |
| EIS+$rh_{surf}$+$rh_{ft}$+$\delta$D+$\Delta\delta$D+q+SST | 0.27 | 0.772 | 0.88 |
| **EIS+$\boldsymbol{\delta}$D+$\boldsymbol{\Delta\delta}$D+q** ***(EIS_ISO Model)*** | 0.267 | 0.778 | 0.88 |
| **EIS+$\mathbf{rh_{surf}}$+$\mathbf{rh_{ft}}$+$\boldsymbol{\delta}$D+$\boldsymbol{\Delta\delta}$D+q+SST+LCF** ***(FULL_ISO Model)*** | 0.263 | 0.784 | 0.89 |

**Table 1.** Metrics for GPR models applied to the estimation of 830 hPa convective moistening tendencies for out-of-sample GCM output from 2010-2011, sorted by RMS error. Each model was trained on output from 2007-2009 with the features indicated. $q$ is the mixing ratio, $\Delta\delta$D the difference between the $\delta$D at a given mixing ratio and Rayleigh distillation to the same mixing ratio, $rh_{surf}$ is the relative humidity in the lowest model level, $rh_{ft}$ is the relative humidity in the lower free troposphere at 830 hPa, $LCF$ is the low-cloud fraction. NO_ISO, EIS_ISO, and FULL_ISO models indicated.

| **Model** | **Training Set** | **Test Set** | **RMSE** | **ADJ R^2** |
|---|---|---|---|---|
| EIS_ISO | AMIP | PI | 0.405 | 0.571 |
| NO_ISO | AMIP | PI | 0.392 | 0.599 |
| FULL_ISO | AMIP | PI | 0.347 | 0.686 |
| EIS_ISO | AMIP | 4X | 0.591 | 0.002 |
| NO_ISO | AMIP | 4X | 0.412 | 0.516 |
| FULL_ISO | AMIP | 4X | 0.413 | 0.513 |
| | | | | |
| EIS_ISO | 4X | AMIP | 0.424 | 0.439 |
| NO_ISO | 4X | AMIP | 0.411 | 0.475 |
| FULL_ISO | 4X | AMIP | 0.444 | 0.387 |
| EIS_ISO | 4X | PI | 0.327 | 0.721 |
| NO_ISO | 4X | PI | 0.38 | 0.622 |
| FULL_ISO | 4X | PI | 0.349 | 0.683 |
| EIS_ISO | 4X | 4X | 0.3 | 0.743 |
| NO_ISO | 4X | 4X | 0.204 | 0.881 |
| FULL_ISO | 4X | 4X | 0.202 | 0.883 |
| | | | | |
| EIS_ISO | PI+4X | AMIP | 0.407 | 0.484 |
| NO_ISO | PI+4X | AMIP | 0.345 | 0.63 |
| FULL_ISO | PI+4X | AMIP | 0.367 | 0.58 |
| EIS_ISO | PI+4X | PI | 0.283 | 0.791 |
| NO_ISO | PI+4X | PI | 0.273 | 0.805 |
| FULL_ISO | PI+4X | PI | 0.234 | 0.856 |
| EIS_ISO | PI+4X | 4X | 0.31 | 0.726 |
| NO_ISO | PI+4X | 4X | 0.208 | 0.876 |
| FULL_ISO | PI+4X | 4X | 0.192 | 0.895 |

**Table 2.** Metrics for GPR models trained on different climates as indicated and applied to AMIP, PI, and 4X simulations. Descriptions of EIS_ISO , NO_ISO, and FULL_ISO provided in the text.

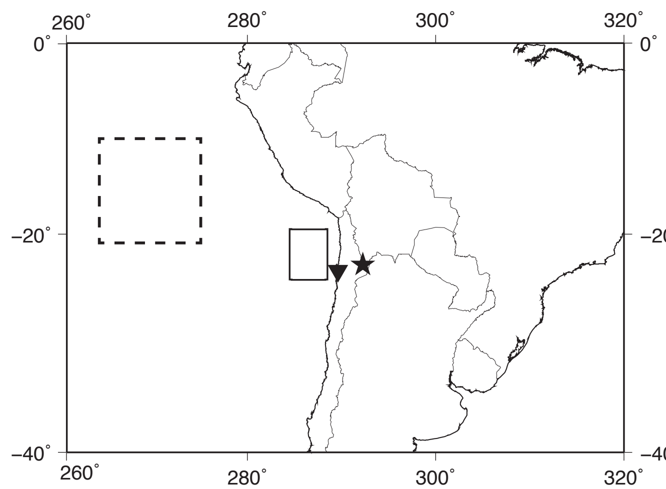


**Figure 1.** Location map of study area. Star and triangle indicate location of Chajnantor Plateau and Antofagasta, respectively. Solid box indicates averaging region for satellite cloud, SST, and humidity data. Dashed box indicates analysis region for LMDZ output.

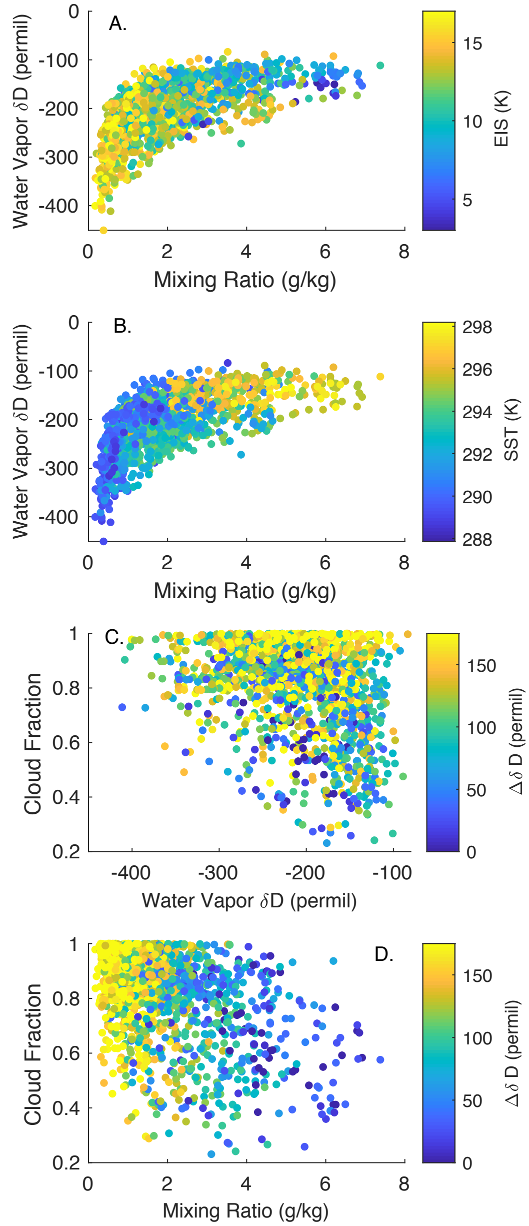


**Figure 2.** Scatterplot of relationships between in-situ water vapor isotopic measurements from the Chajnantor Plateau in northern Chile with (A) EIS, (B) SST, and cloud fraction and $\Delta\delta D$ with (C) $\delta D$ and (D) mixing ratio.

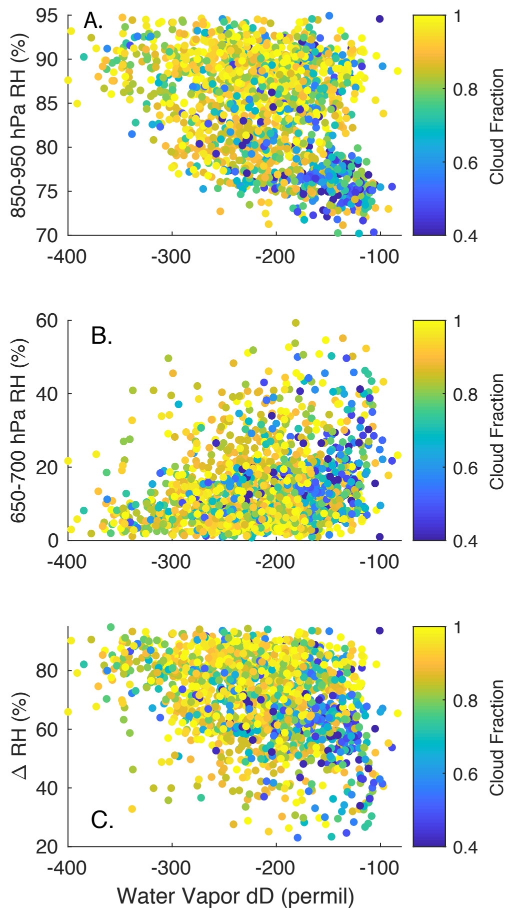


**Figure 3.** Scatterplot of relationships between in-situ water vapor isotopic measurements from the Chajnantor Plateau in northern Chile with SAPHIR relative humidity. (A) $\delta$D versus the RH from the 850 hPa to 950 hPa level; (B) $\delta$D versus the RH from the 650 hPa to 750 hPa level; (C) $\delta$D versus the difference in RH between (A) and (B).

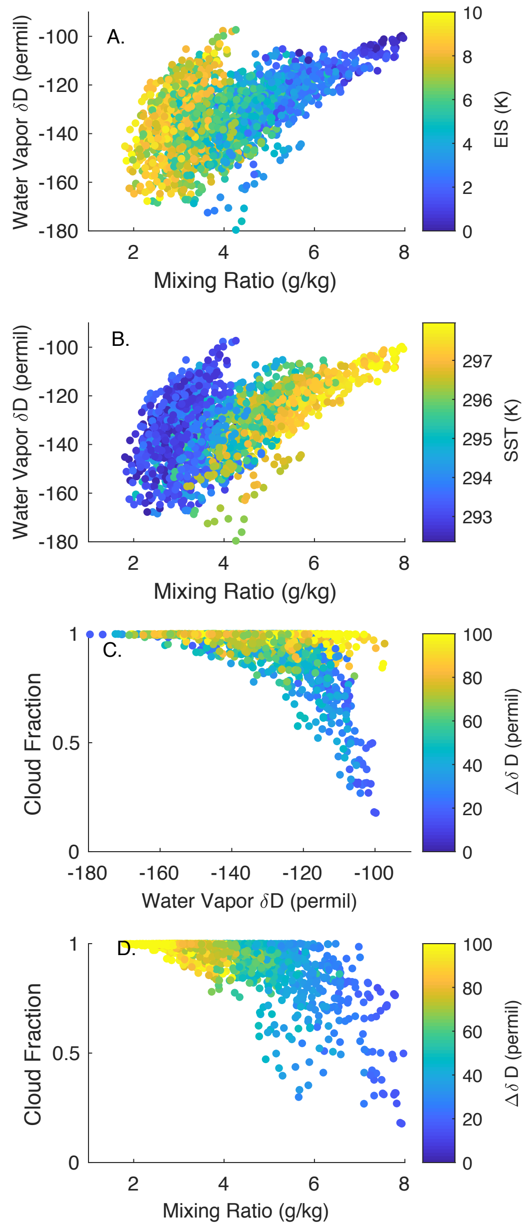


**Figure 4.** As in Figure 2 for LMDZ output from averaging region shown in Figure 1.

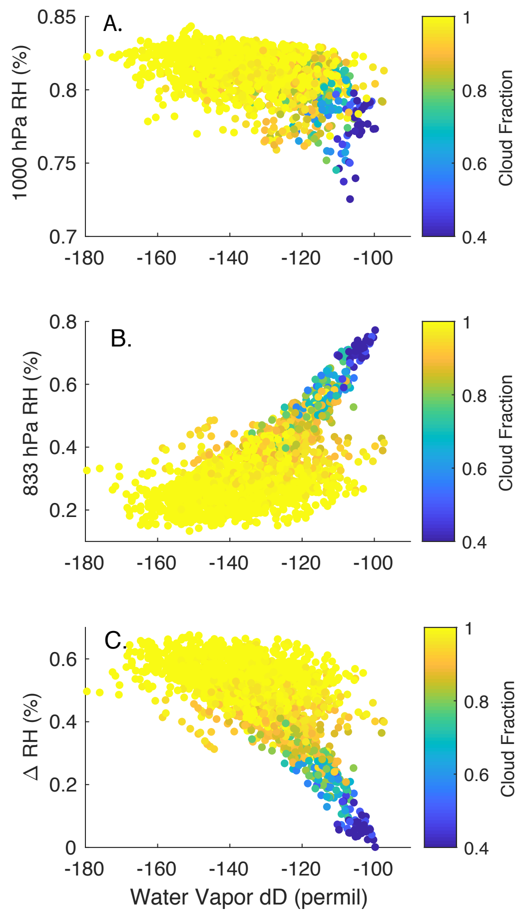


**Figure 5.** As in Figure 3 for LMDZ output from averaging region shown in Figure 1. Water vapor $\delta$D is from 830 hPa for all panels.

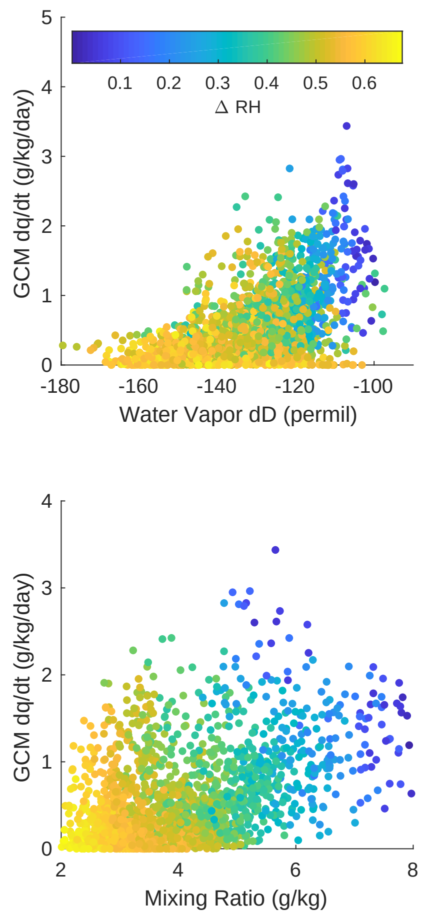


**Figure 6.** Scatterplots of water vapor $\delta$D versus shallow convective moistening tendencies (top) and mixing ratio versus shallow convective moistening tendencies (bottom). Colors are the RH gradient ($\Delta RH$)

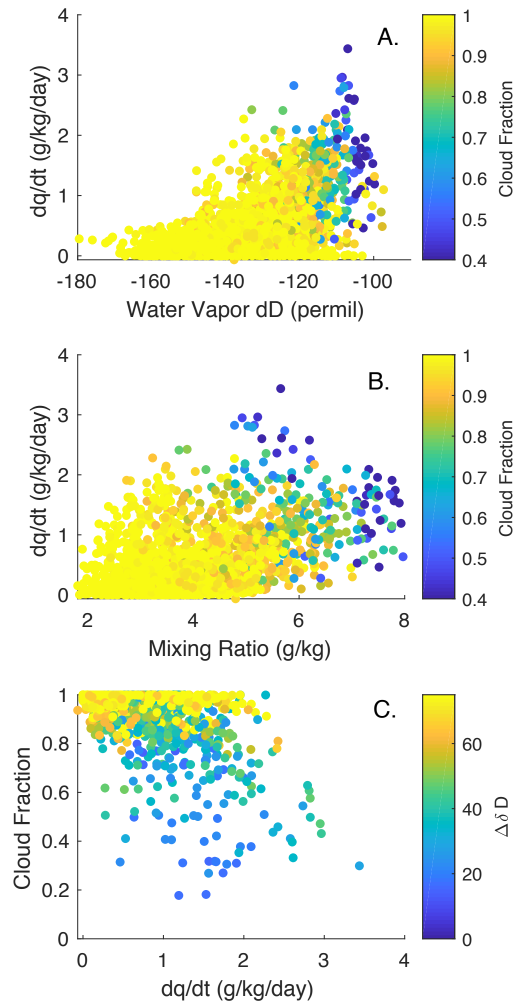


**Figure 7.** Relationships between GCM shallow convective moistening tendencies (dq/dt) and (A) water vapor $\delta$D and LCF; (B) mixing ratio and LCF; (C) LCF and $\Delta\delta$D.

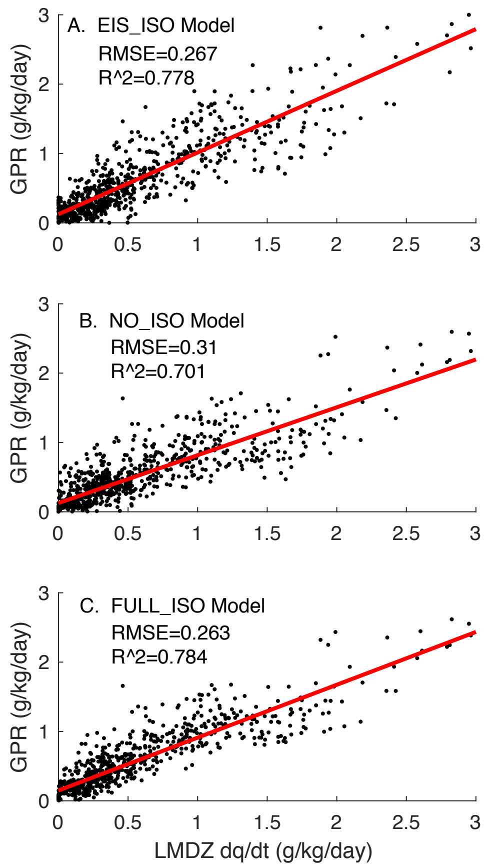


**Figure 8.** Scatterplots and metrics of estimated 830 hPa dq/dt from (A) the EIS_ISO model, (B) the NO_ISO model compared to the GCM output of dq/dt and (C) the FULL_ISO model

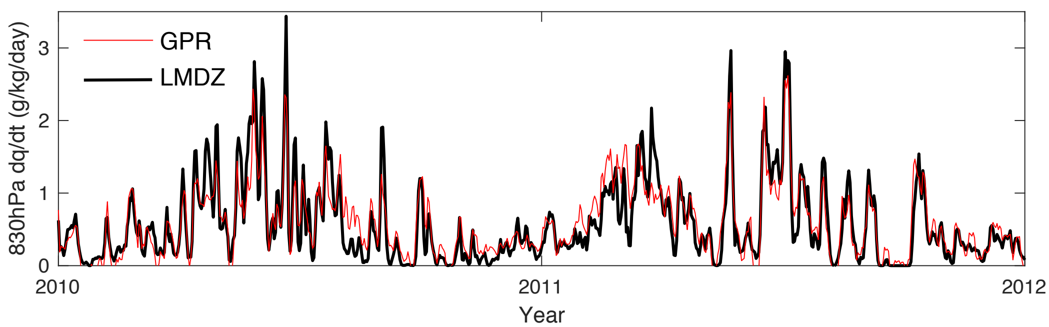


**Figure 9.** Time series of 830 hPa shallow convective moistening tendencies from the GCM (black) and from the FULL_ISO GPR model.

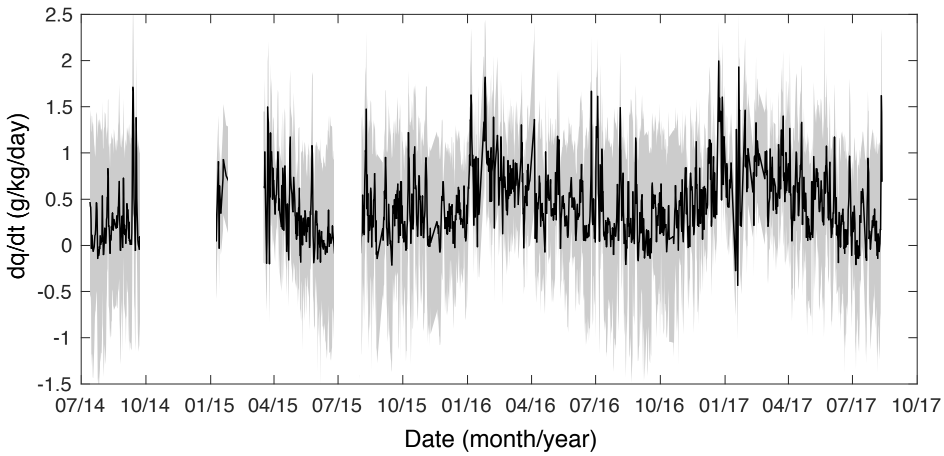


**Figure 10.** Time series of estimated shallow convective dq/dt from FULL_ISO model trained on AMIP simulations, based on input data from in-situ measurements on Chajnantor, soundings from Antofagasta, and remote sensing data from offshore. The gray band shows $\pm 1\sigma$ uncertainty.

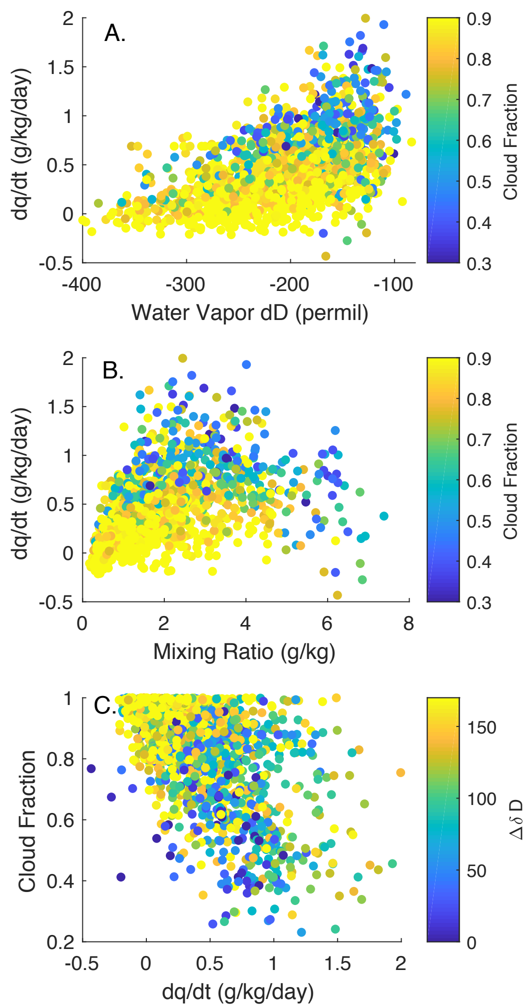


**Figure 11.** As in Figure 7, except for Chajnantor dataset, with dq/dt derived from GPR model.

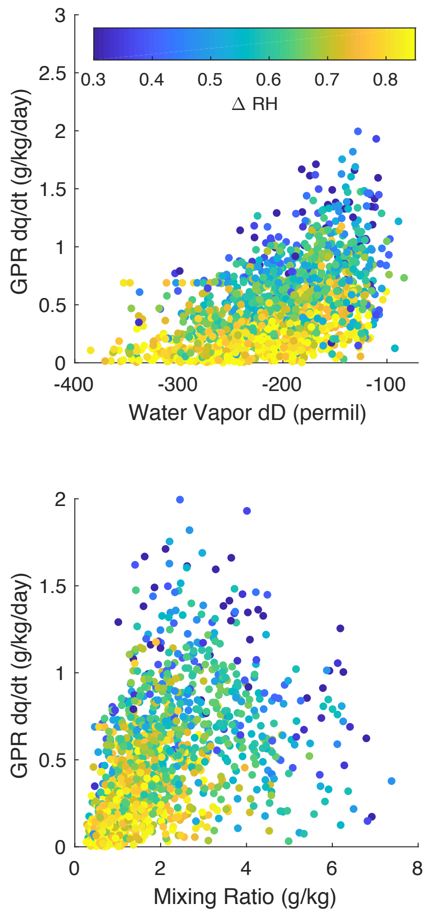


**Figure 12.** As in Figure 6, except for Chajnantor dataset, with dq/dt derived from GPR model.

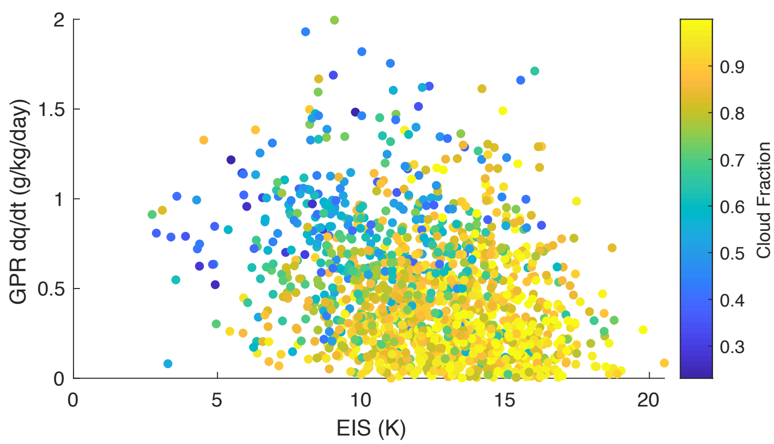


**Figure 13.** Relationships between EIS, GPR-derived moistening tendencies, and cloud fraction.